CMS Physics Analysis Summary

Search for long-lived heavy neutral leptons decaying in the CMS muon detectors in proton-proton collisions at $\sqrt{s} = 13$ TeV

The CMS Collaboration

Abstract

A search for heavy neutral leptons (HNLs) decaying in the CMS muon system is presented. The data sample consists of 137 fb^{-1} of proton-proton collisions at $\sqrt{s} = 13$ TeV, recorded at the LHC in 2016–2018. Decay products of long-lived HNLs could interact with the shielding materials in the CMS muon system and create hadronic and electromagnetic showers detected by the muon chambers. This distinctive signature provides a unique handle to search for HNLs with masses below 10 GeV and proper decay lengths of the order of meters. The signature is sensitive to HNL couplings to all three generations of leptons. Candidate events are required to contain a prompt electron or muon and a shower in the muon chambers. No significant deviations from the standard model background expectation are observed, and the most stringent limits to date are found for HNLs in the mass range of 2.1–3.0 (1.9–3.3) GeV, reaching squared mixing parameter values as low as 8.9×10^{-6} (4.6×10^{-6}) in the electron (muon) channel.

1 Introduction

The observation of neutrino oscillations [1–3] provides experimental evidence for nonzero neutrino masses [4]. Cosmological considerations [5, 6] and direct measurements [7] imply that the neutrino masses are much smaller than the masses of other standard model (SM) fermions and the vacuum expectation value of the Higgs potential, hinting at an alternative mechanism for generating the masses of neutrinos.

One possible explanation is the existence of heavy neutral leptons (HNLs) with right-handed chirality, giving rise to the gauge-invariant mass terms for the SM neutrinos through the "seesaw" mechanism [8–15]. The HNLs are singlets with respect to the SM gauge groups and therefore do not interact with SM particles through the electroweak or strong interactions, but can be produced through mixing with the SM electron, muon, and tau neutrinos [16, 17]. There can be distinct HNL particles and antiparticles (Dirac type) or the HNL can be its own antiparticle (Majorana type). An HNL (N) is characterized by its mass, m_N, and its mixing matrix elements V_{Ne}, $V_{N\mu}$, and $V_{N\tau}$, with electrons, muons, and tau leptons, respectively. The HNL lifetime is inversely proportional to $m_N^5 |V_{N\ell}|^2$ [18], with $\ell = e, \mu, \tau$, and can be macroscopically long-lived for sufficiently low coupling strengths. Models with HNLs are well motivated because they can explain the baryon asymmetry of the universe through CP violation in the HNL system [19, 20], provide a dark matter candidate [21], and explain the observed anomalous magnetic moment of the muon [22].

Past searches for HNLs have covered a wide range of masses ranging from a few keV to several TeV [23–25]. At the LHC, searches conducted by the ATLAS, CMS, and LHCb Collaborations [26–32] have targeted prompt and long-lived HNL decays.

In this note, a search for Dirac and Majorana HNLs with mean proper decay lengths ($c\tau_0$) in the range of 0.1–10 m is performed. A data sample collected by the CMS experiment in 2016–2018 and corresponding to an integrated luminosity of $137\,\text{fb}^{-1}$ is used in this search. An HNL that decays via a virtual W boson can result in a final state with two charged leptons and a neutrino or one lepton and two quarks. Figure 1 shows the Feynman diagram for the production of HNL via a W boson, where the prompt lepton from the W boson serves as a clean signature for triggering. We search for HNLs decays occurring within the muon detector system of the CMS experiment. These decays would produce a particle shower as the HNL decay products interact with the steel shielding material of the CMS muon detectors. This process results in the striking signature of a localized high-multiplicity cluster of muon detector hits. Because of the macroscopic distance from the primary interaction point to the CMS muon detectors and its large volume of geometric acceptance, this signature is sensitive to a large class of models involving long-lived particles (LLPs) and uniquely sensitive to HNLs with $c\tau_0$ above 0.1 m and enables to extend the search sensitivity to unprecedented low couplings in the m_N range of 1–3 GeV.

The outline of the note is as follows: a brief description of the CMS detector is given in Section 2. The data set and the simulated samples of events are detailed in Section 3, followed by a description of the event selection and categorization in Section 4. A description of the backgrounds and the method used to estimate them is given in Section 5. A summary of the sources of systematic uncertainties affecting the expected number of signal and background events can be found in Section 6. The results and interpretations are presented in Section 7 followed by a summary of the note in Section 8.
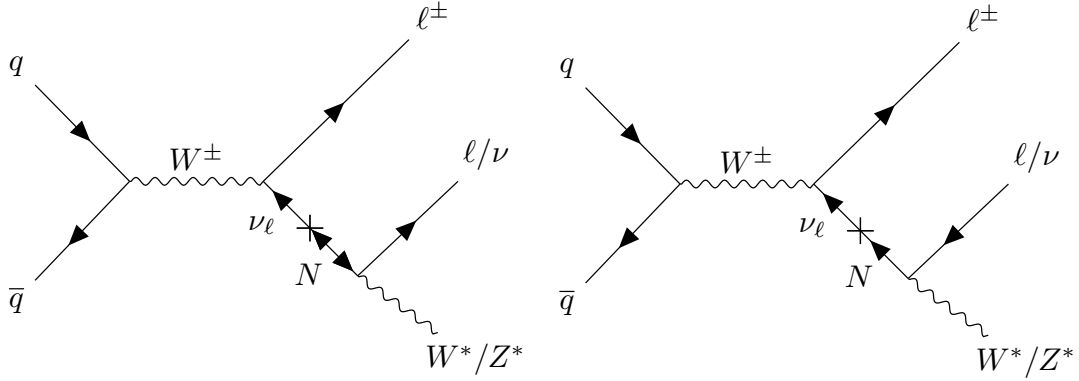
Figure 1: Feynman diagrams for the production of a Majorana (left) and a Dirac (right) HNL via a W boson decay and through its mixing with an SM neutrino. The prompt lepton from the W boson serves as a clean signature for triggering, while the decay products of the HNL are reconstructed as a cluster of muon detector hits.

2 The CMS detector

The central feature of the CMS detector is a superconducting solenoid of 6 m internal diameter, providing a magnetic field of 3.8 T. Within the solenoid volume are a silicon pixel and strip tracker, a lead tungstate crystal electromagnetic calorimeter (ECAL), and a brass and scintillator hadron calorimeter (HCAL), each composed of a barrel and two endcap sections.

The ECAL consists of 75 848 lead tungstate crystals, which cover $|\eta| < 1.48$ in the barrel region and $1.48 < |\eta| < 3.00$ in the two endcap regions. The excellent signal-to-noise ratio and stable pulse shape of the ECAL sensors allow for timing measurements with the best resolution achievable at very large energies of better than 100 ps per hit [33]. The HCAL is composed of cells of width 0.087 in η and azimuth (ϕ, in radians) for the region $|\eta| < 1.74$, progressively increasing to a maximum of 0.174 for larger values of $|\eta|$, along with the forward calorimeters extending the η coverage provided by the barrel and endcap detectors. Muons are measured in the range $|\eta| < 2.4$, with detection planes embedded in the steel flux-return yoke outside the solenoid and made using three technologies: drift tubes (DTs), cathode strip chambers (CSCs), and resistive-plate chambers (RPCs).

The barrel DT chambers are located in regions of pseudorapidity $|\eta| < 1.2$ and are organized into 4 stations, labeled MB1 to MB4. Each station comprises a ring of chambers assembled between two layers of the steel flux-return yoke and is divided along the beam axis into 5 wheels. The stations are located approximately 4, 5, 6, and 7 m away from the interaction point radially (r). In the first 3 stations, every DT chamber consists of 3 "superlayers" (SLs), each comprising 4 staggered layers of parallel DT cells, giving a total of 12 layers. The innermost and outermost SLs measure the charge particle position in the r-ϕ plane, while the middle SL measures the position in the longitudinal plane. The chambers in the last station (MB4) contain only two SLs that measure positions in the r-ϕ plane. The DT cells are designed to provide a uniform electric field such that the position of traversing charged particles can be inferred from measured arrival time and the constant drift velocity.

The CSC detector covers a region of pseudorapidity between $|\eta| = 0.9$ and 2.4 and is composed of four stations in each endcap, labeled ME1 to ME4, which are rings of chambers interleaved between two layers of steel-flux return yoke at approximately the same value of z. The stations are located approximately 7, 8, 9.5, and 10.5 m away from the interaction point along the beam-

line axis on both ends of the detector. Each chamber consists of six layers containing cathode strips along the radial direction and anode wires perpendicular to the strips. Position, as well as timing, information of traversing charged particles are extracted from the electrical signals on the anode wires and the cathode strips on each chamber.

The RPC detectors are placed alongside the DT and CSC detector chambers, and are primarily designed to provide timing information for the muon trigger. RPC chambers in the barrel are labeled RB and those in the endcap are labeled RE.

Events of interest are selected using a two-tiered trigger system. The first level, composed of custom hardware processors, uses information from the calorimeters and muon detectors to select events at a rate of around 100 kHz within a fixed latency of about 4 μs [34]. The second level, known as the high-level trigger, consists of a farm of processors running a version of the full event reconstruction software optimized for fast processing, and reduces the event rate to around 1 kHz before data storage [35]. A more detailed description of the CMS detector, together with a definition of the coordinate system used and the relevant kinematic variables, can be found in Ref. [36].

3 Simulated samples

Signal samples for HNL production are generated at leading order (LO) with the Monte Carlo (MC) generator MADGRAPH5_aMC@NLO [37–40]. The simulated events at the matrix element level are interfaced with PYTHIA 8.226 [41] to simulate the shower and hadronization of partons, and the underlying event description. Only the W production channel is considered in the simulated signal samples. The signal sample is generated at the leading order for W boson production, and up to two additional partons are considered in the matrix element calculations for the generation of the HNL samples. The MLM jet matching scheme [42] is used.

The branching ratio of W boson decays into an HNL plus a lepton is proportional to the square of the coupling strength $V_{N\ell}$, where ℓ could be e, μ, or τ. The signature considered in this search is sensitive to mixing with ν_e, ν_μ, or ν_τ since the decay products of the HNL in the muon detector system are reconstructed as particle showers. The final states consist of one prompt lepton (e or μ) and HNL decay products. To account for higher order effects, the cross sections of the signal samples are assumed to be the next-to-next-to-LO W boson production cross section, which is 20508.9 ± 770.9 pb [43] including the branching ratio to leptons, multiplied by the square of the HNL mixing matrix elements.

Signals corresponding to both Dirac and Majorana HNLs are considered in this search, focusing on $c\tau_0$ in the range of 0.1–10 m. Lepton number violating (LNV) decays are possible for Majorana HNLs, while only lepton number conserving (LNC) decay channels are available for Dirac HNLs. This distinction implies that the width of the Dirac HNL is exactly half of that of the Majorana's case if the HNLs has the same m_N and mixing matrix, and therefore the lifetime of the Dirac HNL will be twice of the Majorana ones [40]. Since in this search, the charged leptons from the decays of the HNL are reconstructed as a cluster in the muon detector system, the final states from LNV events and LNC events are indistinguishable. Therefore, the signal yields of a simulated Majorana sample are used to be interpreted as a Dirac HNL one with twice the lifetime.

Generated events are processed through a simulation of the detector geometry and response using GEANT4 [44]. The same reconstruction software is applied to both data and simulated events. Generated events are simulated using an expected distribution of the number of ad-

ditional pp interactions within the same or nearby bunch crossings (pileup). All generated events are reweighted such that the distribution of the number of collisions per bunch crossing matches the one observed in data, with an average of approximately 23 (32) interactions per bunch crossing [45–47] in 2016 (2017–2018). Simulated samples use the underlying event tune CUETP8M1 [48] in 2016 and the CP5 tune [49] in 2017–2018.

The HNL signal samples were generated for m_N in the range of 1 GeV to 4 GeV and $c\tau_0$ in the range of 100 mm to 10 m. Since only a discrete set of lifetimes was generated, the signal predictions for intermediate lifetimes were estimated by performing a reweighting procedure described below. The HNLs are assumed to couple exclusively to one of the three SM neutrino families with different mixing probabilities $|V_{N\ell}|^2$, depending on m_N. The signal production cross section and lifetimes are determined by the values of m_N and $|V_{N\ell}|^2$, which in turn determine the signal acceptance and reconstruction efficiency. For a fixed value of m_N, therefore, a simple cross section rescaling is not sufficient to correctly reproduce the behavior of other HNLs with same m_N and different $|V_{N\ell}|^2$. To emulate an HNL signal sample with a specific value of $|V_{N\ell}|^2$, we thus apply per-event weights to the events such that the HNL lifetime distribution (taken before the parton shower and detector simulation) matches the predicted distribution for the chosen $|V_{N\ell}|^2$ value. For signal scenarios with m_N in between the masses of the simulation samples generated, we calculate the signal yield prediction interpolating between the predictions from the simulated samples at nearby m_N based on the fact that the acceptance to the muon system differs only through the Lorentz-boost factor.

To obtain a more accurate description of the boost of the HNL signal, we reweight the W p_T spectrum of the signal MC samples to DYTURBO [50].

4 Event reconstruction and selection

The objects in each event are reconstructed using the particle-flow (PF) algorithm [51], which identifies each individual particle in an event as an electron, photon, muon, charged or neutral hadron, with an optimized combination of information from the various elements of the CMS detector. The resulting particles are referred to as PF candidates. Electrons are identified as a primary charged particle track and potentially many ECAL energy clusters corresponding to this track extrapolation to the ECAL and to possible bremsstrahlung photons emitted along the way through the tracker material [52]. The electron momentum is estimated by combining the energy measurement in the ECAL with the momentum measurement in the tracker. Muons are identified as tracks in the central tracker consistent with either a track or several hits in the muon system, and associated with calorimeter deposits compatible with the muon hypothesis [53]. Photons are identified as ECAL energy clusters not linked to the extrapolation of any charged particle trajectory to the ECAL [54]. The energy of photons is obtained from the ECAL measurement. Charged hadrons are identified as charged particle tracks neither identified as electrons, nor as muons. The energy of charged hadrons is determined from a combination of the track momentum and the corresponding ECAL and HCAL energies, corrected for the response function of the calorimeters to hadronic showers. Finally, neutral hadrons are identified as HCAL energy clusters not linked to any charged hadron trajectory, or as a combined ECAL and HCAL energy excess with respect to the expected charged hadron energy deposit. The energy of neutral hadrons is obtained from the corresponding corrected ECAL and HCAL energies.

To identify the electrons and muons from the decay of the W boson, we impose additional selection requirements to enhance the signal purity of these objects. For electron candidates,

requirements are imposed on the shape of the electromagnetic shower in the ECAL, the quality of the matching between the track trajectory and the ECAL shower, and isolation from additional particles near the candidate. A tight working point for this electron identification is used, which has an average efficiency of 70%. We consider electron candidates with $p_T > 30$ GeV and $|\eta| < 2.5$; a more stringent requirement $p_T > 35$ GeV is imposed for the data collected in 2017–2018 to match the increased p_T threshold on the single electron trigger from 27 to 32 GeV. For muon candidates, requirements are imposed on the quality of the track in the silicon tracker, the global compatibility of the hits in the silicon tracker and muon detector comprising the muon candidate, and isolation from additional particles near the candidate. The tight working point is required, which has an efficiency above 95%. We consider muon candidates with $p_T > 25$ GeV and $|\eta| < 2.4$; a more stringent requirement $p_T > 28$ GeV is imposed for the data collected in 2017 to match the increased p_T threshold on the single muon trigger from 24 to 27 GeV.

In this search, jets are used to veto muon detector shower cluster objects that are within $\Delta R < 0.4$ of the cluster to suppress punch-through jet background. Jets are reconstructed by clustering PF candidates using the anti-k_T algorithm [55, 56] with a distance parameter of 0.4. Additional proton-proton interactions within the same or nearby bunch crossings (pileup) can contribute additional tracks and calorimetric energy depositions to the jet momentum. To mitigate this effect, charged particles identified to be originating from pileup vertices are discarded and an offset correction is applied to correct for remaining contributions [57]. Jet energy corrections are derived from simulation studies so that the average measured energy of jets becomes identical to that of particle level jets. In situ measurements of the momentum balance in dijet, photon + jet, Z + jet, and multijet events are used to determine any residual differences between the jet energy scale in data and in simulation, and appropriate corrections are made [58]. Additional selection criteria are applied to each jet to remove jets potentially dominated by instrumental effects or reconstruction failures [57]. To select a top quark sample used in the background prediction, we identify jets originating from a heavy-flavor parton using the medium working point of the combined secondary vertex algorithm [59, 60].

The missing transverse momentum vector $\vec{p}_T^{\text{miss}}$ is computed as the negative vector sum of the transverse momenta of all the PF candidates in an event, and its magnitude is denoted as p_T^{miss} [61]. The primary vertex (PV) is taken to be the vertex corresponding to the hardest scattering in the event, evaluated using tracking information alone, as described in Section 9.4.1 of Ref. [62].

We select data events triggered by the single electron or single muon triggers and require the events to have one and only one prompt electron or prompt muon candidates satisfying the identification and isolation criteria described above. To further suppress the background from SM events composed uniquely of jets produced through the strong interaction, referred to as quantum chromodynamics (QCD) multijet events, we require $p_T^{\text{miss}} > 30$ GeV. The above requirements are designed to select events with the production of W boson, through which the HNL signal could be produced.

4.1 Muon detector shower clusters

For long-lived particles that decay within or just prior to the DT and CSC muon detectors, the material in the iron return yoke structure can induce a particle shower, creating a geometrically localized and isolated cluster of hits. We cluster these hits by means of the DBSCAN algorithm [63] using their η and ϕ coordinates, with $\Delta R = 0.2$ as the distance parameter, and require a minimum of 50 hits per cluster. The number of reconstructed hits comprising the

cluster is defined as (N_hits). These cluster objects, which we defined as muon detector shower (MDS) objects, are rarely produced by SM background processes and they are used in this search as a powerful signature to distinguish LLP signal from background.

The efficiency for MDS objects to be reconstructed depends on whether the LLP decays primarily to hadrons, including the hadronic decay of taus, or to muons or electrons and photons. Typically, clusters with more hits are produced by hadrons, resulting in a higher MDS reconstruction efficiency for LLPs that decay hadronically compared to LLPs that decay mostly to electrons and photons. For hadronic decays, the reconstruction efficiency is about 80% and for electrons and photon decays efficiency is about 35–45%, depending on whether the MDS is reconstructed in CSC or DT.

To suppress background MDS clusters produced by energetic SM particles that traverse the shielding material between the tracking volume and the muon detectors without being stopped, a process that we refer to as jet "punchthrough" from here on, we veto any MDS clusters in the DT (CSC) detector whose centroid lies within $\Delta R < 0.4$ to an AK4 jet with p_T larger than 20 (10) GeV. To suppress background MDS clusters produced by muon bremsstrahlung, we impose a tighter veto on any MDS clusters in the DT (CSC) detector whose centroid lies within $\Delta R < 0.8$ to a muon candidate with p_T larger than 10 (20) GeV. The p_T thresholds for the jet and muon vetos were chosen to yield optimal signal to background discrimination, and differ due to the different amount of shielding present. With the jet and muon vetos applied, the MDS clusters typically have no PF candidates with large transverse momentum pointing in the same direction, and thus are expected to be correlated to the direction of the $\vec{p}_\text{T}^{\,\text{miss}}$ vector for signal events.

Muons with trajectories pointing towards two regions of the detector corresponding to the chimneys of the CMS detector cavern have highly reduced reconstruction efficiency due to less detector coverage as the space near the chimneys are taken by cables and other services going up through the chimneys. As a result, the rate of background MDS clusters produced by muon bremsstrahlung and passing the muon veto is significantly increased. To suppress these backgrounds, we veto any clusters whose centroid is within $\Delta R < 0.3$ to the following two locations in η and ϕ coordinates: ($\eta = 0.3$, $\phi = 1.7$) or ($\eta = -0.3$, $\phi = 1.15$), which corresponds to the locations of the chimneys.

The rate of background MDS clusters caused by jet punchthrough is significantly larger for clusters with hits in the muon detector station closest to the interaction point because of the much reduced amount of shielding material. Furthermore, any hits observed in the stations between the interaction point and the station containing the majority of the cluster hit is indicative of jet punchthrough, while signal LLPs are neutral and therefore do not produce any hit before they decay.

To further suppress such jet punchthrough backgrounds, we veto any MDS clusters in the CSCs whose centroid lies within $\Delta R < 0.4$ to any hits observed in the RB1, ME-11, ME-12, or RE1/2 stations or any segments in the MB1 station. Segments are required in the MB1 station rather than single hits due to the larger rate of noise in the DT detectors, which would produce a larger signal inefficiency for such a veto. For MDS clusters in the DTs, we veto any cluster whose centroid lies within $\Delta R < 0.5$ with more than 1 hits observed in the MB1 station and we require less than 8 MB1 hits in the adjacent wheels within $\Delta\phi < \pi/4$.

After the jet and muon vetos, the dominant background is due to clusters from pileup, including the out-of-time pileup, which is not in the same bunch crossing of the primary vertex. To eliminate the background clusters from out-of-time pileup, we reconstruct a cluster time for

the clusters in both CSC and DT detectors. For CSC clusters, the cluster time is reconstructed from the mean time of the hits comprising the cluster, where the time of each hit is calibrated to result in a distribution centered at value 0 ns for the triggering bunch crossing. To suppress background clusters we require that the cluster time is between -5 and 12.5 ns and that the root-mean-square spread of the timestamps of hits comprising the cluster is less than 20 ns. The design time resolution of CSC chambers is about 6 ns. Because hits in the DT detector do not have a time measurement that is independent from its position measurement, we require that DT clusters match to at least one hit in the RPC detector in the same wheel and with $|\Delta\phi| < 0.5$ to the cluster centroid. Each matching RPC hit measures one bunch crossing value, and the most frequently appearing bunch crossing value of the matching RPC hits is defined as the cluster time. The cluster time is required to match to the bunch crossing corresponding to the PV.

Finally, for CSC clusters we require additional cluster identification requirements that were developed in Ref. [64], where we make successively smaller $|\eta|$ requirements as the number of CSC stations containing hits and the distance between the station and the primary interaction point decrease. This CSC cluster identification algorithm has ~60% efficiency and suppresses the background by a factor of 8.

We observed anomalous detector noise in specific components of the DT detectors for a certain period of data taking, which produced an anomalously large rate of background MDS clusters. To suppress this noise-induced background, we have vetoed MDS clusters comprising of hits detected in those particular DT chambers taken during the affected time period. This veto represents less than 0.1% of the total luminosity.

After requiring all the vetos on the cluster, we require the events to contain at least one CSC or DT hit cluster with at least 50 hits. The minimum number of hits is chosen to be larger than the number of hits that a muon is expected to create in CSC or DT. The presence of the MDS signature along with the associated vetos and identification criteria suppresses standard model background by a factor exceeding 10^7, while typical signal efficiencies are 25-35%.

5 Background estimation

After the event selections described in Section 4, the dominant source of background is the W+jets process producing the prompt lepton and hadrons from pileup, recoil, or underlying event producing the cluster. For this type of background, the azimuthal angle between the prompt lepton and the cluster centroid ($\Delta\phi_{lep}$) is near uniformly distributed and is independent of N_{hits}, as the cluster and lepton are produced from two independent processes. Therefore, we use the ABCD method using the $\Delta\phi_{lep}$ and N_{hits} to estimate the contribution from W+jets process. The search region is separated into four bins A, B, C, and D as illustrated in Figure 2. Since the HNL is primarily produced back-to-back with the prompt lepton, the bin with the best signal to background ratio is bin D with $\Delta\phi_{lep} > 2.8$ and $N_{\text{hits}} > 150$ or 200; the bin with $\Delta\phi_{lep} > 2.8$ and $N_{\text{hits}} \leq 150$ or 200 is defined as bin C; the bin with $\Delta\phi_{lep} \leq 2.8$ and $N_{\text{hits}} > 150$ or 200 is defined as bin A; and the bin containing the least signal is bin B with $\Delta\phi_{lep} \leq 2.8$ and $N_{\text{hits}} \leq 150$ or 200. The bin boundaries are optimized for the best expected search sensitivity, separately for each of the search categories. The response of the DT and CSC detectors to shower particles are generally different with CSC signal clusters having a larger hit multiplicity compared to DT signal clusters. The optimal bin boundary is found to be higher (200) for the CSC signal region (SR) compared to the DT signal regions (150). The background yield in the most signal enriched bin D is predicted to be $N_{\text{pred.,D}} = (N_A N_C)/N_B$, where N_X is the background yield in each bin X. Any background process that obeys this relationship is

defined as the ABCD background. To account for a potential signal contribution to bins A, B, and C, a binned maximum likelihood fit is performed simultaneously in the four bins, with a common signal strength parameter scaling the signal yields in each bin. The background component of the fit is constrained to obey the ABCD relationship.
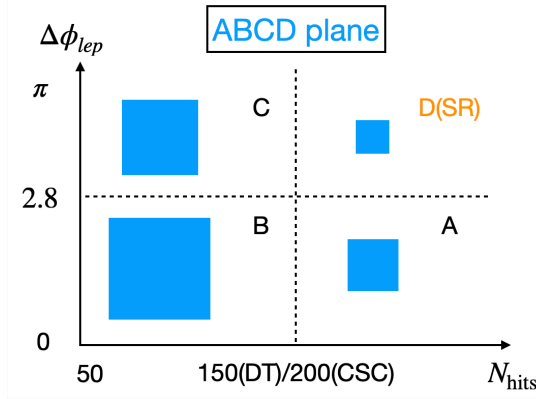

Figure 2: Definition of the ABCD plane. The size of the blue boxes illustrates the relative amount of expected events in each of the bins, with bin B and C having the majority of the event yields. Bin D is the signal region (SR).

As background size and composition are different between the events with a selected prompt electron and prompt muon, we consider these two types of events in separate categories. We also separate events with clusters in the CSC or DT detectors into separate categories. Finally, for events in the category with a prompt muon and a MDS cluster in the DT detector, we separate events into subcategories DT-MB2 and DT-MB3/4 categories, depending on whether the majority of hits in the cluster fall in the MB2 station or the subsequent stations of the DT detector. This subcategorization is motivated by the fact that the background size and composition is different for clusters in the MB2 station due to thinner shielding in front of it. This results in a total of 5 signal regions.

The ABCD background estimation procedure is validated using events in the early out-of-time (OOT) validation region (VR), defined as events passing all analysis cuts except the time requirements described in Section 4.1 and required to have a negative cluster time. Additionally, the background estimation procedure is validated in the in-time VR, defined as events with azimuthal angle between the MDS cluster centroid position and the $\vec{p}_T^{\mathrm{miss}}$, $\Delta\phi(cluster, \vec{p}_T^{\mathrm{miss}}) > 0.7$, which is signal depleted because the MDS and $\vec{p}_T^{\mathrm{miss}}$ are aligned in the same direction, since $\vec{p}_T^{\mathrm{miss}}$ is calculated solely from tracker and calorimeter information and the momentum of the HNL will be undetected. The observed and predicted yields for these validation regions are summarized in Table 1 and show that the ABCD method are consistent with observed background yields.

The ABCD background prediction in the bin D of the signal regions is found in Table 2 for each of the event categories considered in this search. The event yields for the A, B, and C are shown, as well as the prediction for the background in the signal enhanced bin D.

In the prompt muon event categories, $Z \to \mu\mu$ events constitue a significant background source that is not predicted by the ABCD method. One of the two muons decayed from the Z boson may undergo bremsstrahlung in the muon detector and produce an MDS in a back-to-back configuration with respect to the other reconstructed prompt muon, mimicking the configuration for signal. The muon veto suppresses such backgrounds, but in rare cases the muon reconstruction may be inefficient due to instrumental effects such as gaps between chambers.

Table 1: Validation of the ABCD method in the OOT and in-time validation regions.

Event Category	Validation Region	A	B	C	D	$N_{\text{pred.,D}}$
Muon, DT-MB2	OOT	9	6924	944	0	1.23 ± 0.41
Muon, DT-MB3/4	OOT	11	593	86	1	1.60 ± 0.52
Muon, CSC	OOT	103	31074	4044	9	13.40 ± 1.34
Electron, DT	OOT	14	3301	366	2	1.55 ± 0.42
Electron, CSC	OOT	33	13774	1647	2	3.95 ± 0.69
Muon, DT-MB2	In time	10	5087	467	2	0.92 ± 0.29
Muon, DT-MB3/4	In time	9	785	107	2	1.23 ± 0.43
Muon, CSC	In time	31	7445	532	1	2.22 ± 0.41
Electron, DT	In time	8	2446	220	0	0.72 ± 0.26

Table 2: The event yields in the bins A, B, and C are shown in each of the event categories considered in the search, as well as the prefit prediction for the ABCD background in the signal enhanced bin D.

Channel	Region	A	B	C	$N_{\text{pred.,D}}$
Muon	CSC	40	9316	1219	5.2 ± 0.8
Muon	DT-MB2	16	6512	1048	2.6 ± 0.7
Muon	DT-MB3/4	11	1011	229	2.5 ± 0.8
Electron	CSC	10	3993	497	1.2 ± 0.4
Electron	DT	15	3069	463	2.3 ± 0.6

These un-reconstructed muons will lead to $p_{\text{T}}^{\text{miss}}$ in the same direction as the cluster, thus are not validated by the VRs listed in Table 1.

We define a $Z \rightarrow \mu\mu$ control region (CR) by inverting the MB1 or ME11/ME12 hit veto requirements for MDS clusters in the DT or CSC detectors, respectively. After that, bin D will be dominated by the $Z \rightarrow \mu\mu$ background. The $Z \rightarrow \mu\mu$ background yield in bin D of the $Z \rightarrow \mu\mu$ CR is calculated as $N_{Z \rightarrow \mu\mu,\text{D}}^{\text{CR}} = N_{\text{D}}^{\text{CR}} - N_{\text{ABCD bkg,D}}^{\text{CR}}$, where N_{D}^{CR} is the observed data yield in bin D and $N_{\text{ABCD bkg,D}}^{\text{CR}}$ is the ABCD method prediction. We extrapolate $N_{Z \rightarrow \mu\mu,\text{D}}^{\text{CR}}$ to the signal region, defining a transfer factor ζ, which estimates the relative efficiency for MDS clusters produced by muon bremsstrahlung to pass and fail the MB1 and ME11/ME12 veto requirements.

The transfer factor ζ is measured in a sample enhanced in MDS clusters produced by muon bremsstrahlung obtained by selecting dileptonic decays of top quark pairs. We select events with one prompt electron matched to an electron trigger object, no reconstructed muon, one MDS cluster passing all of the veto selections except the MB1 or ME11/12 vetos, and two and only two additional jets with $p_{\text{T}} > 20\,\text{GeV}$, $|\eta| < 2.4$ and passing the CSV-v2 medium b-tag selection. We also require that the MDS cluster is geometrically separated by $\Delta R > 0.8$ from any of the jets to ensure that the MDS cluster is not produced by jet punchthrough. These jet requirements result in an event sample that is pure in dileptonic top quark pair events, thus ensuring that the MDS cluster is produced by the unreconstructed muon. We measure the transfer factors separately for MDS clusters in the DT and CSC detectors. We observed a linear dependence of the transfer factor on N_{hits} in the MB2 category. To account for this dependence, we perform a linear fit to the data in the control region and evaluate the fitted function at $N_{\text{hits}} = 150$ as the transfer factor for the MB2 category. Finally, the $Z \rightarrow \mu\mu$ background contribution to bin D of the signal region is calculated as $N_{Z \rightarrow \mu\mu,\text{D}}^{\text{SR}} = \zeta \times N_{Z \rightarrow \mu\mu,\text{D}}^{\text{CR}}$. Details of the $Z \rightarrow \mu\mu$ background prediction are summarized in Table 3.

To validate the $Z \rightarrow \mu\mu$ background estimation method, we defined a validation region as a subset of the MB2 signal region with cluster size < 120, with negligible signal contributions. In this validation region, we define the bin boundaries for the ABCD method to be at 2.8 in $\Delta\phi_{lep}$ and at 110 in N_{hits}. We perform the prediction of the $Z \rightarrow \mu\mu$ and ABCD background using the exact same method applied to the full signal region and obtain predictions of 2.7 ± 1.6 for the $Z \rightarrow \mu\mu$ background and 9.9 ± 1.3 for the ABCD background, for a total background prediction of 12.6 ± 2.1. We observe an event yield of 12, demonstrating that our methods accurately predict both types of backgrounds.

Table 3: Summary of the $Z \rightarrow \mu\mu$ background estimate in different categories. The first three columns shows estimates in the $Z \rightarrow \mu\mu$ enriched control region, and the last two columns show the transfer factors ζ to predict the $Z \rightarrow \mu\mu$ background in the signal region.

Region	N_D^{CR}	$N_{\text{ABCD bkg,D}}^{CR}$	$N_{Z\rightarrow\mu\mu,D}^{CR}$	ζ	$N_{Z\rightarrow\mu\mu,D}^{SR}$
CSC	129	45 ± 2	84 ± 12	$(4.8\pm1.3)\%$	3.9 ± 1.2
DT MB2	35	12.2 ± 1.5	22.8 ± 6.1	$(36\pm31)\%$	8.2 ± 7.4
DT MB3/4	6	2.9 ± 0.7	3.1 ± 2.6	$(2\pm1)\%$	0.06 ± 0.06

6 Systematic uncertainties

The dominant systematic uncertainties for this search are the uncertainties on the background predictions. The main source of uncertainty for the ABCD backgrounds arises from the statistical uncertainty of the background-enriched bins A, B, and C. This uncertainty accounts for 27% and 22% of the size of the total background in the electron and muon category, respectively, for MDS clusters in the DT detector, and 40% and 18% of the size of the total background in the electron and muon category, respectively, for MDS clusters in the CSC detector.

For the prompt muon categories, the uncertainty on the estimate of the $Z \rightarrow \mu\mu$ background also contributes to the total uncertainty significantly. The uncertainty for that background prediction arises from the statistical uncertainty of the transfer factor measurement, accounting for about 72%, 2% and 15% of the size of the total background in the muon channel for DT-MB2, DT-MB3/4 and CSC clusters, respectively.

Systematic uncertainties on the signal include both theoretical and instrumentation effects. We propagate the uncertainty on the signal yield due to the theoretical uncertainty in the prediction of the W boson production cross section and for the shape of the W boson p_{T} distribution. The uncertainty of W boson p_{T} distribution is evaluated by varying the renormalization and factorization scales and evaluating the size of the envelope in the resulting signal yield, which is found to be 1.6%. The inclusive cross section of W boson production has an uncertainty of 3.8%, dominated by the PDF uncertainty.

The accuracy of the simulation prediction for the cluster reconstruction efficiency relies on its ability to model correctly the response of the muon detectors in an environment with multiple particles, each producing a large number of secondary shower particles. The uncertainties on the cluster reconstruction efficiency for both CSC and DT clusters are evaluated using a $Z \rightarrow \mu\mu$ data sample, where clusters are produced when one of the muons undergoes bremsstrahlung and the associated photon produces an electromagnetic shower, and they account for 16% and 13% of the signal yield for the DT and CSC categories, respectively. Data-to-simulation corrections on other cluster properties are also derived with the same method, and the uncertainty of the corrections are propagated as systematic uncertainties. For DT clusters, a correction of 6.8%

is applied for the MB1 veto efficiency with an uncertainty of 7.4%. For CSC clusters, corrections of 2.8%, 6.8%, and 2.1% are applied to account for the hit and segment vetos, muon veto and jet veto efficiencies, with the uncertainties of 0.1%, 4.5%, and 0.06%, respectively. Additionally, the uncertainty of the CSC cluster identification, time and time spread requirements are found to be 5%, 0.9% and 2.8% respectively. In the signal simulations, the condition of reading out CSC reconstructed hits is assumed to be satisfied, whereas in data-taking, only those reconstructed hits that have at least two cathode hits at different CSC layers and matching a given predefined patterns of hits are read out. This could lead to an underestimation of the efficiency of ME11/12 veto in simulation, which we estimated to have an uncertainty of 1%.

We also propagate a number of standard systematic uncertainties that have a minor impact on the signal yield prediction. They include the pileup and luminosity uncertainty, the jet energy scale uncertainty, and the prompt electron or muon trigger and the selection efficiencies. Finally, the statistical uncertainty from the limited number of simulated events used to calculate the signal yield prediction is also propagated and ranges between 5 and 10% depending on the m_N and lifetime. A full list of systematic uncertainties affecting the predicted signal yield is summarized in Table 4.

Table 4: Summary of systematic uncertainties affecting the signal yield prediction. For DT clusters, the systematics uncertainties due to jet and muon vetos are found to be negligible, and are omitted.

Systematic Uncertainty	Object	Size of unc.
Luminosity	—	1.6%
Pile-up	—	1%
W cross section	—	3.8%
W p_T	—	1.6%
Trigger	Muon	<0.1%
Identification	Muon	0.4–0.5%
Isolation	Muon	0.2–0.6%
Trigger	Electron	0.2–0.3%
Identification	Electron	2.2–8.0%
Jet energy scale	MET	2.0%
Cluster reconstruction	CSC cluster	13%
Cut-based ID	CSC cluster	5.1%
Jet veto	CSC cluster	0.06%
Muon veto	CSC cluster	4.5%
CSC readout	CSC cluster	1.0%
Hits and segment veto	CSC cluster	0.1%
Cluster time	CSC cluster	0.9%
Cluster time spread	CSC cluster	2.8%
Cluster reconstruction	DT cluster	16%
MB1 veto	DT cluster	7.4%

7 Results and interpretation

Figure 3 shows the expected and observed number of events in the signal regions of the different event categories and the corresponding background predictions. The observed yields agree overall with the predicted background in all channels.
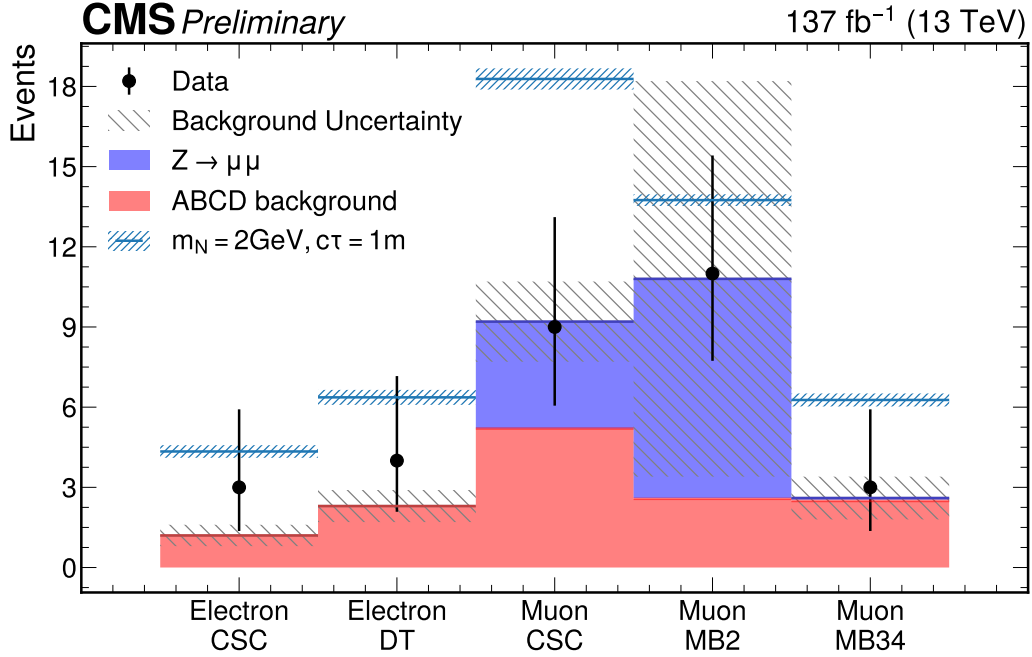
Figure 3: The expected and observed number of events in the signal region (bin D) of different event categories. Signal yields of a 2 GeV Majorana HNL with the mean proper decay length of 1 m are also overlayed on top of the expected background.

In the absence of an excess of data events over the background prediction, exclusion limits on the HNL production cross sections are evaluated using a modified frequentist approach [65–67], with the binned profile likelihood ratio as the test statistics. The likelihood is constructed as the product of Poisson distributions of observed events with a mean value of predicted events in each bin of the ABCD plane, across all 5 event categories. The predicted events in each bin include the background yields predicted with the ABCD method, plus the $Z \rightarrow \mu\mu$ background contribution for bin D and the signal yields obtained from simulated events. Systematic uncertainties of the predicted events are included in the likelihood as nuisance parameters with Gaussian constraints. The asymptotic formulae [68] are used to evaluate the exclusion limits for each HNL signal scenarios. The asymptotic assumption is validated to be consistent with toy-based evaluation of the exclusion limits.

Due to the lower p_{T} thresholds for the prompt muon, the signal yields in the muon channel is larger than that of the electron channels for the same m_{N} and lifetime. However, the presence of the $Z \rightarrow \mu\mu$ background reduces the overall sensitivity of the muon channel to a comparable level to the electron channel. For both the muon and electron channel, the CSC category contributes the majority of overall sensitivity. This is due to the fact that CSC has smaller backgrounds compared to the DT clusters, hence retaining more signal events at the optimal thresholds for background.

Figure 4 and 5 show the expected and observed upper limits at 95% confidence level (CL) on HNL coupling strengths ($|V_{\mathrm{Ne}}|^2$, $|V_{\mathrm{N}\mu}|^2$, and $|V_{\mathrm{N}\tau}|^2$) as a function of m_{N} for Majorana and Dirac HNL interpretation respectively. For $|V_{\mathrm{Ne}}|^2$ ($|V_{\mathrm{N}\mu}|^2$), only events passing the electron (muon) selections are used to evaluated the limits. For $|V_{\mathrm{N}\tau}|^2$, events selected with both the electron and muon selections are used, since the prompt tau-lepton can decay into electrons

or muons. The limits of $|V_{N\ell}|^2$ versus m_N feature an upper branch and a lower branch, which corresponds to HNL with short and long lifetimes. The low acceptance in the short lifetime branch is compensated with the increased cross section to reach similar signal yields as the long lifetime branch. Below m_N of 2 (1.5) GeV for electron/muon (tau)-type HNL, we do not set a limit in the short lifetime branch as the signal acceptance in the muon system approaches zero due to the short lifetime of the HNL. This search extends the existing limits towards the parameter space with longer lifetimes or smaller $|V_{N\ell}|^2$. Table 5 summarizes the most stringent observed limits of $|V_{N\ell}|^2$ for Majorana and Dirac type HNL in this search. More stringent limits have been set below m_N of 1 GeV by other experiments [23]. Between 1 GeV and 1.9 (2.1) GeV, the CHARM [69] experiment sets stringent limits on muon (electron) couplings. Above 3.3 (3.0) GeV, previous CMS results [30, 70] place tighter limits on muon (electron) couplings.

Table 5: Summary of the most stringent observed limits of $|V_{N\ell}|^2$ for Majorana and Dirac type HNL in this search.

Coupling	HNL type	m_N (GeV)	Excluded range at 95% CL
$|V_{Ne}|^2$	Majorana	2.6	8.6×10^{-6}–5.0×10^{-5}
$|V_{N\mu}|^2$	Majorana	2.8	5.0×10^{-6}–3.9×10^{-5}
$|V_{N\tau}|^2$	Majorana	1.8	2.5×10^{-4}–1.8×10^{-3}
$|V_{Ne}|^2$	Dirac	2.8	8.9×10^{-6}–7.5×10^{-5}
$|V_{N\mu}|^2$	Dirac	3.3	4.6×10^{-6}–2.8×10^{-5}
$|V_{N\tau}|^2$	Dirac	1.8	3.1×10^{-4}–5.9×10^{-3}

Since the HNL decay products is reconstructed as a MDS cluster, the reconstruction efficiency is independent of the flavour of the HNL. This allows reweighting signal yields with pure couplings into mixed couplings of different lepton flavours. The relative ratios between the coupling strengths ($|V_{Ne}| : |V_{N\mu}| : |V_{N\tau}| \equiv f_e : f_\mu : f_\tau$) are constrained to sum to unity for a given m_N and $c\tau_0$. Figure 6 shows the limits on the HNL mass and mean proper decay length as a function of relative coupling to the three lepton generations.

8 Summary

A search for long-lived Dirac or Majorana heavy neutral leptons (HNL) has been performed using proton-proton collision data at $\sqrt{s} = 13$ TeV, corresponding to an integrated luminosity of 137 fb^{-1}, using events with one prompt electron or muon and a muon detector shower (MDS) resulting from the HNL decay occurring in the CMS muon detector. The presence of the MDS signature along with the associated vetos and identification criteria suppresses the standard model background by a factor exceeding 10^7. No significant excess over the standard model backgrounds is observed. The results are interpreted as 95% confidence level limits on the HNL mixing parameters V_{Ne}, $V_{N\mu}$, and $V_{N\tau}$. We set the most stringent limits to date for HNLs in the mass range of 2.1–3.0 (1.9–3.3) GeV, reaching squared mixing parameter values as low as 8.6×10^{-6} (4.6×10^{-6}) in the electron (muon) channel.

References

[1] Super-Kamiokande Collaboration, "Evidence for oscillation of atmospheric neutrinos", *Phys. Rev. Lett.* **81** (1998) 1562, doi:10.1103/PhysRevLett.81.1562, arXiv:hep-ex/9807003.
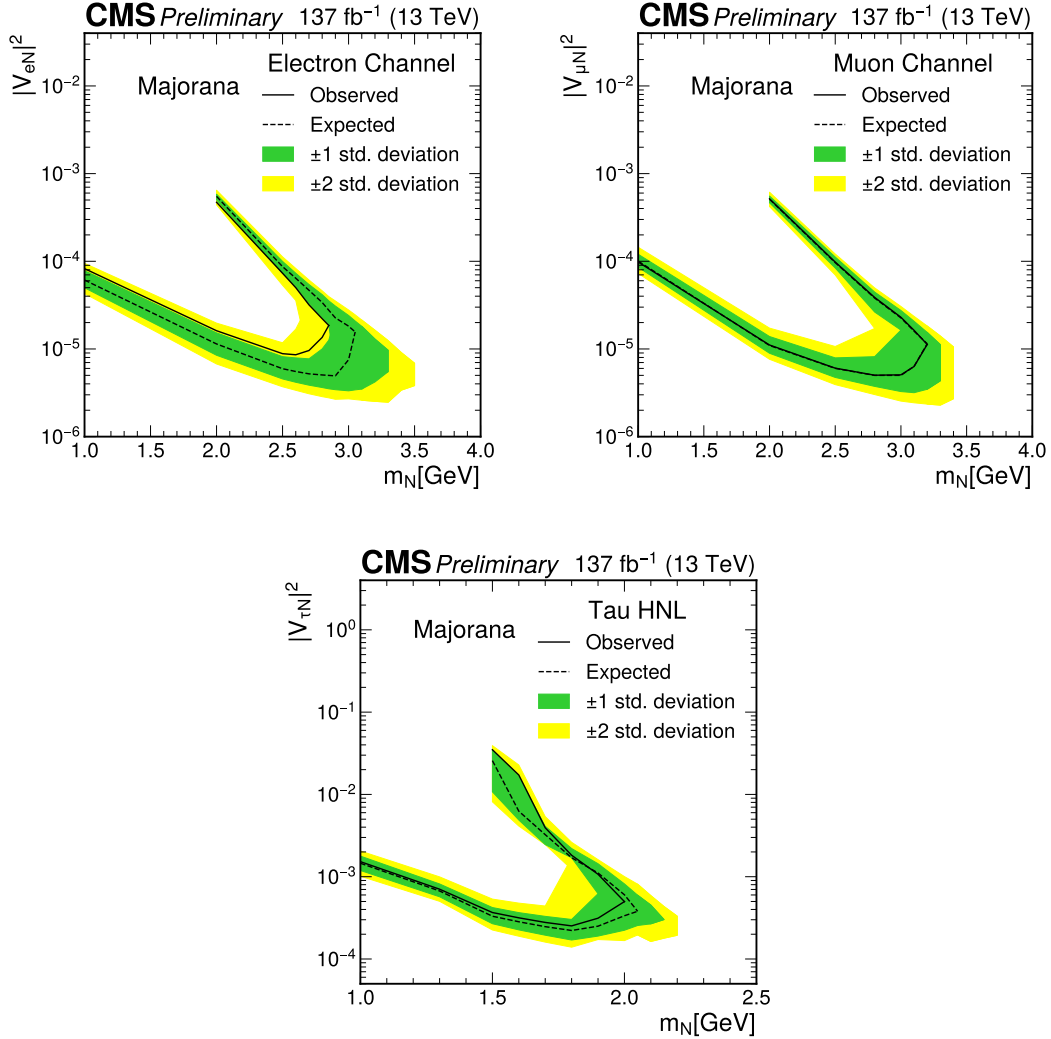
Figure 4: Expected and observed upper 95% CL limits on Majorana HNL production as a function of the HNL mass (m_N) and coupling strengths on pure electron coupling (top left), pure muon coupling (top right) and pure tau coupling. The tau-coupling limit is obtained by combining the results from the electron channel and muon channel. No limit is set below m_N of 2 (1.5) GeV and above $|V_{N\ell}|^2$ of 5.2×10^{-4} (3.5×10^{-2}) for electron/muon (tau)-type HNL as the signal acceptance to the muon system approaches zero due to the short lifetime of the HNL.

[2] SNO Collaboration, "Direct evidence for neutrino flavor transformation from neutral-current interactions in the Sudbury Neutrino Observatory", *Phys. Rev. Lett.* **89** (2002) 011301, `doi:10.1103/PhysRevLett.89.011301`, `arXiv:nucl-ex/0204008`.

[3] KamLAND Collaboration, "First results from KamLAND: Evidence for reactor antineutrino disappearance", *Phys. Rev. Lett.* **90** (2003) 021802, `doi:10.1103/PhysRevLett.90.021802`, `arXiv:hep-ex/0212021`.

[4] S. Bilenky, "Neutrino oscillations: From a historical perspective to the present status", *Nucl. Phys. B* **908** (2016) 2, `doi:10.1016/j.nuclphysb.2016.01.025`, `arXiv:1602.00170`.
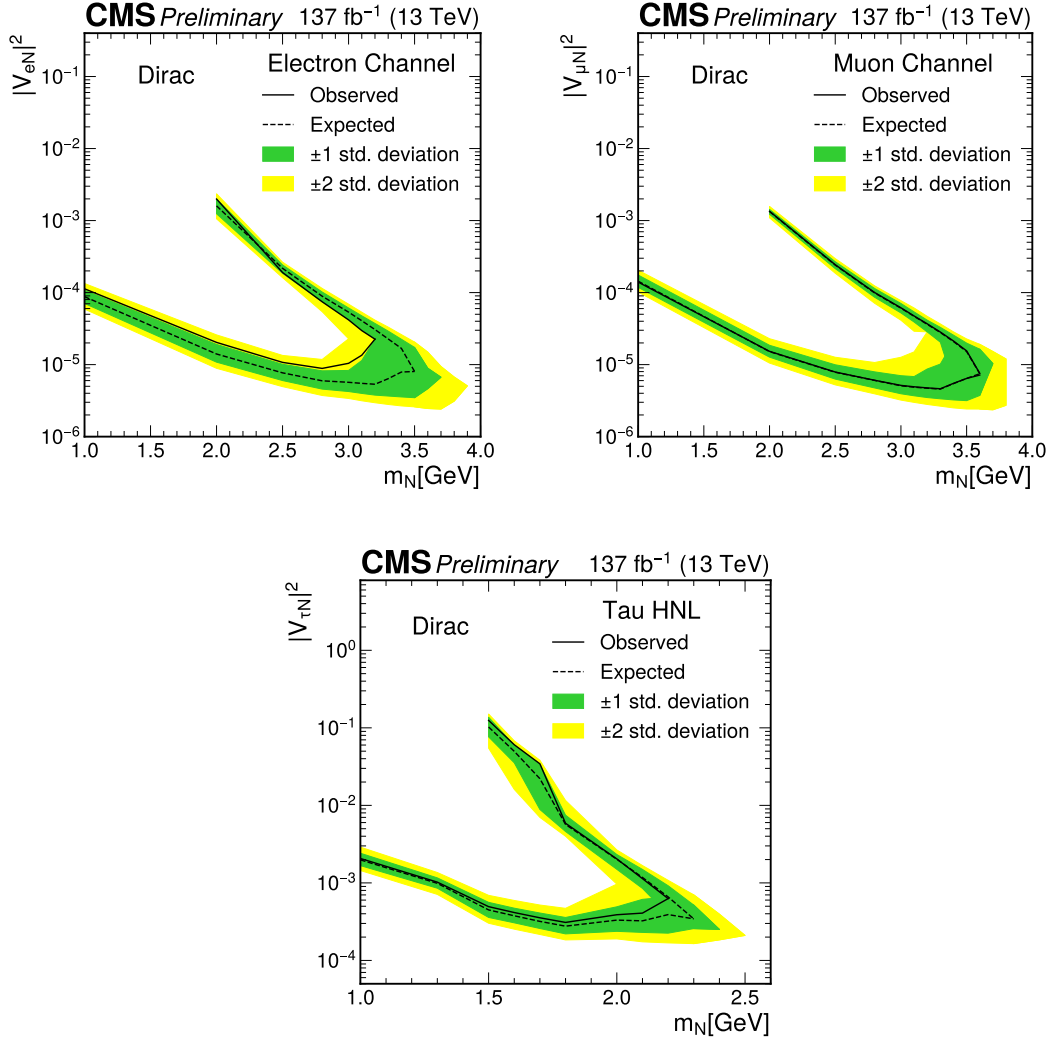
Figure 5: Expected and observed upper 95% CL limits on Dirac HNL production as a function of the HNL mass (m_N) and coupling strengths on pure electron coupling (top left), pure muon coupling (top right) and pure tau coupling. The tau-coupling limit is obtained by combining the results from the electron channel and muon channel. No limit is set below m_N of 2 (1.5) GeV and above $|V_{N\ell}|^2$ of 1.3×10^{-3} (1.2×10^{-1}) for electron/muon (tau)-type HNL as the signal acceptance in the muon system approaches zero due to the short lifetime of the HNL.

[5] S. Roy Choudhury and S. Hannestad, "Updated results on neutrino mass and mass hierarchy from cosmology with Planck 2018 likelihoods", *JCAP* **07** (2020) 037, `doi:10.1088/1475-7516/2020/07/037,arXiv:1907.12598`.

[6] M. Ivanov, M. Simonović, and M. Zaldarriaga, "Cosmological parameters and neutrino masses from the final Planck and full-shape BOSS data", *Phys. Rev. D* **101** (2020) 083504, `doi:10.1103/PhysRevD.101.083504,arXiv:1912.08208`.

[7] J. Formaggio, A. de Gouvêa, and R. Robertson, "Direct measurements of neutrino mass", *Phys. Rept.* **914** (2021) 1, `doi:10.1016/j.physrep.2021.02.002`, `arXiv:2102.00594`.
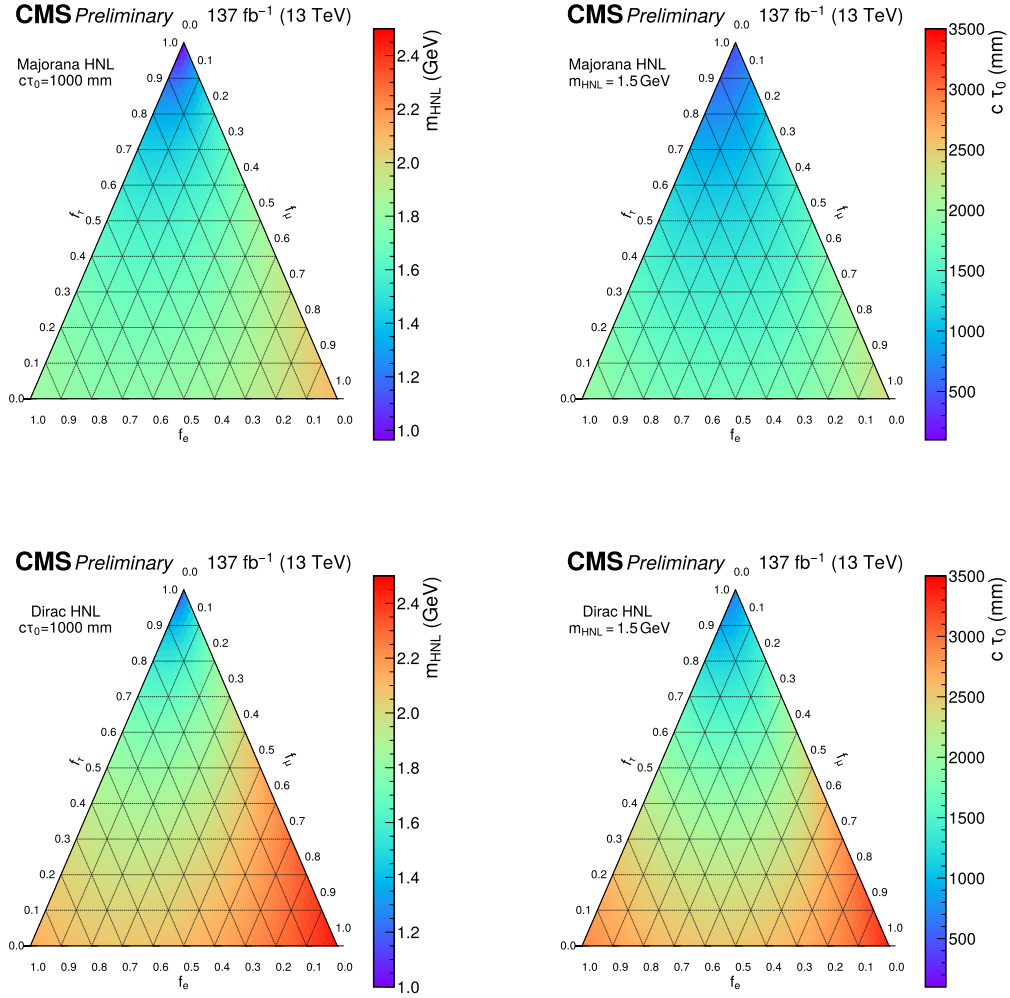
Figure 6: Observed upper 95% CL limits on the Majorana (top) and Dirac (bottom) HNL mass (left) and mean proper decay length (right) as a function of relative coupling to the three lepton generations, considering a mean proper decay length of 1 m and a fixed mass of 1.5 GeV respectively.

[8] P. Minkowski, "$\mu \to e\gamma$ at a rate of one out of 10^9 muon decays?", *Phys. Lett. B* **67** (1977) 421, doi:10.1016/0370-2693(77)90435-X.

[9] T. Yanagida, "Horizontal gauge symmetry and masses of neutrinos", in *Proc. Workshop on the Unified Theories and the Baryon Number in the Universe: Tsukuba, Japan, February 13–14, 1979*. 1979. [Conf. Proc. C 7902131 (1979) 95].

[10] M. Gell-Mann, P. Ramond, and R. Slansky, "Complex spinors and unified theories", in *Supergravity*, p. 315. North Holland Publishing, 1979. arXiv:1306.4669.

[11] S. Glashow, "The future of elementary particle physics", *NATO Sci. Ser. B* **61** (1980) 687, doi:10.1007/978-1-4684-7197-7_15.

[12] R. Mohapatra and G. Senjanović, "Neutrino mass and spontaneous parity nonconservation", *Phys. Rev. Lett.* **44** (1980) 912, doi:10.1103/PhysRevLett.44.912.

[13] J. Schechter and J. Valle, "Neutrino masses in SU(2) ⊗ U(1) theories", *Phys. Rev. D* **22** (1980) 2227, `doi:10.1103/PhysRevD.22.2227`.

[14] R. Shrock, "General theory of weak leptonic and semileptonic decays. I. leptonic pseudoscalar meson decays, with associated tests for, and bounds on, neutrino masses and lepton mixing", *Phys. Rev. D* **24** (1981) 1232, `doi:10.1103/PhysRevD.24.1232`.

[15] Y. Cai, T. Han, T. Li, and R. Ruiz, "Lepton number violation: Seesaw models and their collider tests", *Front. Phys.* **6** (2018) 40, `doi:10.3389/fphy.2018.00040`, `arXiv:1711.02180`.

[16] Z. Maki, M. Nakagawa, and S. Sakata, "Remarks on the unified model of elementary particles", *Prog. Theor. Phys.* **28** (1962) 870, `doi:10.1143/PTP.28.870`.

[17] B. Pontecorvo, "Neutrino experiments and the problem of conservation of leptonic charge", *Zh. Eksp. Teor. Fiz.* **53** (1967) 1717.

[18] K. Bondarenko, A. Boyarsky, D. Gorbunov, and O. Ruchayskiy, "Phenomenology of GeV-scale Heavy Neutral Leptons", *JHEP* **11** (2018) 032, `doi:10.1007/JHEP11(2018)032`, `arXiv:1805.08567`.

[19] M. Fukugita and T. Yanagida, "Baryogenesis without grand unification", *Phys. Lett. B* **174** (1986) 45, `doi:10.1016/0370-2693(86)91126-3`.

[20] E. Chun et al., "Probing leptogenesis", *Int. J. Mod. Phys. A* **33** (2018) 1842005, `doi:10.1142/S0217751X18420058`, `arXiv:1711.02865`.

[21] A. Boyarsky et al., "Sterile neutrino dark matter", *Progress in Particle and Nuclear Physics* **104** (jan, 2019) 1, `doi:10.1016/j.ppnp.2018.07.004`, `arXiv:1807.07938v2`.

[22] Muon g-2 Collaboration, "Measurement of the Positive Muon Anomalous Magnetic Moment to 0.46 ppm", *Phys. Rev. Lett.* **126** (2021), no. 14, 141801, `doi:10.1103/PhysRevLett.126.141801`, `arXiv:2104.03281`.

[23] F. F. Deppisch, P. S. Bhupal Dev, and A. Pilaftsis, "Neutrinos and Collider Physics", *New J. Phys.* **17** (2015), no. 7, 075019, `doi:10.1088/1367-2630/17/7/075019`, `arXiv:1502.06541`.

[24] J. Beacham et al., "Physics Beyond Colliders at CERN: Beyond the Standard Model Working Group Report", *J. Phys. G* **47** (2020), no. 1, 010501, `doi:10.1088/1361-6471/ab4cd2`, `arXiv:1901.09966`.

[25] DELPHI Collaboration, "Search for neutral heavy leptons produced in z decays", *Z. Phys. C* **74** (1997) 57, `doi:10.1007/s002880050370`. [Erratum: `doi:10.1007/BF03546181`].

[26] ATLAS Collaboration, "Search for heavy neutral leptons in decays of W bosons produced in 13 TeV pp collisions using prompt and displaced signatures with the ATLAS detector", *JHEP* **10** (2019) 265, `doi:10.1007/JHEP10(2019)265`, `arXiv:1905.09787`.

[27] ATLAS Collaboration, "Search for heavy neutral leptons in decays of W bosons using a dilepton displaced vertex in $\sqrt{s} = 13$ TeV pp collisions with the ATLAS detector", *submitted to Phys. Rev. Lett.* (4, 2022) `doi:10.48550/arXiv.2204.11988`, `arXiv:2204.11988`.

[28] CMS Collaboration, "Search for heavy neutral leptons in events with three charged leptons in proton-proton collisions at $\sqrt{s} = 13$ TeV", *Phys. Rev. Lett.* **120** (2018), no. 22, 221801, `doi:10.1103/PhysRevLett.120.221801`, `arXiv:1802.02965`.

[29] CMS Collaboration, "Search for heavy Majorana neutrinos in same-sign dilepton channels in proton-proton collisions at $\sqrt{s} = 13$ TeV", *JHEP* **01** (2019) 122, `doi:10.1007/JHEP01(2019)122`, `arXiv:1806.10905`.

[30] CMS Collaboration, "Search for long-lived heavy neutral leptons with displaced vertices in proton-proton collisions at $\sqrt{s}$ =13 TeV", *JHEP* **07** (2022) 081, `doi:10.1007/JHEP07(2022)081`, `arXiv:2201.05578`.

[31] LHCb Collaboration, "Search for heavy neutral leptons in $W^+ \to \mu^+ \mu^\pm$jet decays", *Eur. Phys. J. C* **81** (2021) 248, `doi:10.1140/epjc/s10052-021-08973-5`, `arXiv:2011.05263`.

[32] LHCb Collaboration, "Search for long-lived particles decaying to $e^\pm \mu^\mp \nu$", *Eur. Phys. J. C* **81** (2021), no. 3, 261, `doi:10.1140/epjc/s10052-021-08994-0`, `arXiv:2012.02696`.

[33] CMS Collaboration, "Search for long-lived particles using delayed photons in proton-proton collisions at $\sqrt{s} = 13$ TeV", *Phys. Rev. D* **100** (2019) 112003, `doi:10.1103/PhysRevD.100.112003`, `arXiv:1909.06166`.

[34] CMS Collaboration, "Performance of the CMS Level-1 trigger in proton-proton collisions at $\sqrt{s} = 13$ TeV", *JINST* **15** (2020) P10017, `doi:10.1088/1748-0221/15/10/P10017`, `arXiv:2006.10165`.

[35] CMS Collaboration, "The CMS trigger system", *JINST* **12** (2017) P01020, `doi:10.1088/1748-0221/12/01/P01020`, `arXiv:1609.02366`.

[36] CMS Collaboration, "The CMS experiment at the CERN LHC", *JINST* **3** (2008) S08004, `doi:10.1088/1748-0221/3/08/S08004`.

[37] J. Alwall et al., "The automated computation of tree-level and next-to-leading order differential cross sections, and their matching to parton shower simulations", *JHEP* **07** (2014) 079, `doi:10.1007/JHEP07(2014)079`, `arXiv:1405.0301`.

[38] D. Alva, T. Han, and R. Ruiz, "Heavy Majorana neutrinos from $W\gamma$ fusion at hadron colliders", *JHEP* **02** (2015) 072, `doi:10.1007/JHEP02(2015)072`, `arXiv:1411.7305`.

[39] C. Degrande, O. Mattelaer, R. Ruiz, and J. Turner, "Fully-Automated Precision Predictions for Heavy Neutrino Production Mechanisms at Hadron Colliders", *Phys. Rev. D* **94** (2016) 053002, `doi:10.1103/PhysRevD.94.053002`, `arXiv:1602.06957`.

[40] S. Pascoli, R. Ruiz, and C. Weiland, "Heavy neutrinos with dynamic jet vetoes: multilepton searches at $\sqrt{s}$=14, 27, and 100 TeV", *Journal of High Energy Physics* **2019** (jun, 2019) `doi:10.1007/jhep06(2019)049`, `arXiv:1812.08750`.

[41] T. Sjöstrand et al., "An introduction to PYTHIA 8.2", *Comp. Phys. Comm.* **191** (2015) 159, `doi:10.1016/j.cpc.2015.01.024`, `arXiv:1410.3012`.

[42] J. Alwall et al., "Comparative study of various algorithms for the merging of parton showers and matrix elements in hadronic collisions", *The European Physical Journal C* **53** (dec, 2007) 473, `doi:10.1140/epjc/s10052-007-0490-5`, `arXiv:0706.2569`.

[43] Y. Li and F. Petriello, "Combining QCD and electroweak corrections to dilepton production in the framework of the FEWZ simulation code", *Physical Review D* **86** (nov, 2012) `doi:10.1103/physrevd.86.094034`, `arXiv:1208.5967`.

[44] GEANT4 Collaboration, "GEANT4—a simulation toolkit", *Nucl. Instrum. Meth. A* **506** (2003) 250, `doi:10.1016/S0168-9002(03)01368-8`.

[45] CMS Collaboration, "Precision luminosity measurement in proton-proton collisions at $\sqrt{s} = 13$ TeV in 2015 and 2016 at CMS", *Eur. Phys. J. C* **81** (2021) 800, `doi:10.1140/epjc/s10052-021-09538-2`, `arXiv:2104.01927`.

[46] CMS Collaboration, "CMS luminosity measurement for the 2017 data-taking period at $\sqrt{s} = 13$ TeV", CMS Physics Analysis Summary CMS-PAS-LUM-17-004, 2018.

[47] CMS Collaboration, "CMS luminosity measurement for the 2018 data-taking period at $\sqrt{s} = 13$ TeV", CMS Physics Analysis Summary CMS-PAS-LUM-18-002, 2019.

[48] CMS Collaboration, "Event generator tunes obtained from underlying event and multiparton scattering measurements", *Eur. Phys. J. C* **76** (2016) 155, `doi:10.1140/epjc/s10052-016-3988-x`, `arXiv:1512.00815`.

[49] CMS Collaboration, "Extraction and validation of a new set of CMS PYTHIA8 tunes from underlying-event measurements", *Eur. Phys. J. C* **80** (2020) 4, `doi:10.1140/epjc/s10052-019-7499-4`, `arXiv:1903.12179`.

[50] S. Camarda et al., "DYTurbo: Fast predictions for Drell-Yan processes", *Eur. Phys. J. C* **80** (2020), no. 3, 251, `doi:10.1140/epjc/s10052-020-7757-5`, `arXiv:1910.07049`.

[51] CMS Collaboration, "Particle-flow reconstruction and global event description with the CMS detector", *JINST* **12** (2017) P10003, `doi:10.1088/1748-0221/12/10/P10003`, `arXiv:1706.04965`.

[52] CMS Collaboration, "Electron and photon reconstruction and identification with the CMS experiment at the CERN LHC", *JINST* **16** (2021) P05014, `doi:10.1088/1748-0221/16/05/P05014`, `arXiv:2012.06888`.

[53] CMS Collaboration, "Performance of the CMS muon detector and muon reconstruction with proton-proton collisions at $\sqrt{s} = 13$ TeV", *JINST* **13** (2018) P06015, `doi:10.1088/1748-0221/13/06/P06015`, `arXiv:1804.04528`.

[54] CMS Collaboration, "Performance of photon reconstruction and identification with the CMS detector in proton-proton collisions at $\sqrt{s} = 8$ TeV", *JINST* **10** (2015) P08010, `doi:10.1088/1748-0221/10/08/P08010`, `arXiv:1502.02702`.

[55] M. Cacciari, G. P. Salam, and G. Soyez, "The anti-k_T jet clustering algorithm", *JHEP* **04** (2008) 063, `doi:10.1088/1126-6708/2008/04/063`, `arXiv:0802.1189`.

[56] M. Cacciari, G. P. Salam, and G. Soyez, "FASTJET user manual", *Eur. Phys. J. C* **72** (2012) 1896, `doi:10.1140/epjc/s10052-012-1896-2`, `arXiv:1111.6097`.

[57] CMS Collaboration, "Pileup mitigation at CMS in 13 TeV data", *JINST* **15** (2020) P09018, `doi:10.1088/1748-0221/15/09/P09018`, `arXiv:2003.00503`.

[58] CMS Collaboration, "Jet energy scale and resolution in the CMS experiment in pp collisions at 8 TeV", *JINST* **12** (2017) P02014, `doi:10.1088/1748-0221/12/02/P02014`, `arXiv:1607.03663`.

[59] CMS Collaboration, "Identification of b-quark jets with the CMS experiment", *JINST* **8** (2013) P04013, `doi:10.1088/1748-0221/8/04/P04013`, `arXiv:1211.4462`.

[60] CMS Collaboration, "Identification of heavy-flavour jets with the CMS detector in pp collisions at 13 TeV", *JINST* **13** (2018) P05011, `doi:10.1088/1748-0221/13/05/P05011`, `arXiv:1712.07158`.

[61] CMS Collaboration, "Performance of missing transverse momentum reconstruction in proton-proton collisions at $\sqrt{s} = 13$ TeV using the CMS detector", *JINST* **14** (2019) P07004, `doi:10.1088/1748-0221/14/07/P07004`, `arXiv:1903.06078`.

[62] CMS Collaboration, "Technical proposal for the Phase-II upgrade of the Compact Muon Solenoid", CMS Technical Proposal CERN-LHCC-2015-010, CMS-TDR-15-02, 2015.

[63] M. Ester, H.-P. Kriegel, J. Sander, and X. Xu, "A density-based algorithm for discovering clusters in large spatial databases with noise", in *Proceedings of the Second International Conference on Knowledge Discovery and Data Mining*, p. 226. Association for the Advancement of Artificial Intelligence, 1996.

[64] CMS Collaboration, "Search for Long-Lived Particles Decaying in the CMS End Cap Muon Detectors in Proton-Proton Collisions at $\sqrt{s}$ =13 TeV", *Phys. Rev. Lett.* **127** (2021), no. 26, 261804, `doi:10.1103/PhysRevLett.127.261804`, `arXiv:2107.04838`.

[65] T. Junk, "Confidence level computation for combining searches with small statistics", *Nucl. Instrum. Meth. A* **434** (1999) 435, `doi:10.1016/S0168-9002(99)00498-2`, `arXiv:hep-ex/9902006`.

[66] A. L. Read, "Presentation of search results: the CL_s technique", *J. Phys. G* **28** (2002) 2693, `doi:10.1088/0954-3899/28/10/313`.

[67] The ATLAS Collaboration, The CMS Collaboration, The LHC Higgs Combination Group, "Procedure for the LHC Higgs boson search combination in Summer 2011", Technical Report CMS-NOTE-2011-005, ATL-PHYS-PUB-2011-11, 2011.

[68] G. Cowan, K. Cranmer, E. Gross, and O. Vitells, "Asymptotic formulae for likelihood-based tests of new physics", *Eur. Phys. J. C* **71** (2011) 1554, `doi:10.1140/epjc/s10052-011-1554-0`, `arXiv:1007.1727`. [Erratum: `doi:10.1140/epjc/s10052-013-2501-z`].

[69] CHARM Collaboration, "A Search for Decays of Heavy Neutrinos in the Mass Range 0.5-GeV to 2.8-GeV", *Phys. Lett. B* **166** (1986) 473, `doi:10.1016/0370-2693(86)91601-1`.

[70] CMS Collaboration, "Search for long-lived heavy neutral leptons with lepton flavour conserving or violating decays to a jet and an electron, muon, or tau lepton", CMS Physics Analysis Summary CMS-PAS-EXO-21-013, 2023.